HHS Public Access

Author manuscript

Phys Biol. Author manuscript; available in PMC 2017 September 21.

Published in final edited form as:

Phys Biol. 2011 October ; 8(5): 056008. doi:10.1088/1478-3975/8/5/056008.

A Microfabricated Magnetic Force Transducer-Microaspiration System for Studying Membrane Mechanics

D J Stark[1,2], **T C Killian**[1], and **R M Raphael**[2]

[1]Department of Physics & Astronomy, Rice University, Houston, TX 77005

[2]Department of Bioengineering, Rice University, Houston, TX 77030

Abstract

The application of forces to cell membranes is a powerful method for studying membrane mechanics. To apply controlled dynamic forces on the piconewton scale, we designed and characterized a microfabricated magnetic force transducer (MMFT) consisting of current-carrying gold wires patterned on a sapphire substrate. The experimentally measured forces applied to paramagnetic and ferromagnetic beads as a function of applied current agree well with theoretical models. We used this device to pull tethers from micro-aspirated giant unilamellar vesicles and measure the threshold force for tether formation. In addition, the interlayer drag coefficient of the membrane was determined from the tether-return velocity under magnetic force-free conditions. At high levels of current, vesicles expanded as a result of local temperature changes. A finite element thermal model of the MMFT provided absolute temperature calibration, allowing determination of the thermal expansivity coefficient of stearoyl-oleoyl-phosphatidycholine vesicles ($1.7 \pm 0.4x10^{-3}$ K^{-1}) and characterization of the Joule heating associated with current passing through the device. This effect can be used as a sensitive probe of temperature changes on the microscale. These studies establish the MMFT as an effective tool for applying precise forces to membranes at controlled rates and quantitatively studying membrane mechanical and thermo-mechanical properties.

Key Terms

Membrane tether formation; thermal expansivity coefficient; interlayer drag viscosity; adhesion; membrane curvature; giant unilamellar vesicle

4. Introduction

Mechanical forces regulate a host of biological processes, and the controlled application of forces to membranes and cells is necessary to study mechanosensitive phenomena such as cell adhesion, mechanotransduction, and stem cell differentiation [1]. Several techniques have been developed for applying localized forces to cells, such as atomic force microscopy (AFM), optical tweezers, and magnetic tweezers [2]. While these techniques have greatly advanced the field of cell and membrane mechanics, they are not without limitations. For

Corresponding Author: Robert M. Raphael, 6500 Main St., MS-142 Rice University, Houston, TX 77030 (phone) 713-348-3494 (fax) 713-348-5877. rraphael@rice.edu.

example, the applied forces are usually not known *a priori*, and as quantitative biology advances, there is an increasing need for accurate knowledge of both the magnitude and the rate at which forces are applied. Moreover, many force application techniques are limited to cells attached to a microscope coverslip. Optical tweezers generally require a high numerical aperture lens to form the optical trap [3], with lower depth of field that limits working distance [4]. AFM experiments are difficult to perform and interpret on cells that are not supported by a substrate.

For these reasons, it can often be practically difficult to apply piconewton forces while simultaneously manipulating cells with micropipettes, such as during microaspiration and patch clamp experiments. Such integrated experiments are necessary for studies that require simultaneous control of a global parameter such as membrane tension or transmembrane voltage and application of a point force. For example, cell adhesion is mediated by receptor-ligand interactions whose strength is dependent on membrane tension [5] and the rate of force application [6]. Thus, a full biophysical understanding of adhesive interactions requires methods for simultaneous control of membrane tension and application of precise forces.

Early studies in cell adhesion noted that when adherent red blood cells were subject to fluid forces, long, thin tubes of membrane (termed tethers) formed [7]. Later, controlled tether formation became a powerful tool for systematic studies of cell and membrane mechanical properties [8, 9]. In particular, tether experiments utilizing giant unilamellar vesicles (GUVs) provided a direct method to measure the membrane bending stiffness [10, 11], which regulates processes that involve dramatic changes in membrane curvature such as membrane fusion and microvilli formation. Tether experiments were also developed to measure dynamic membrane properties such as the interlayer drag coefficient opposing relative motion of the membrane leaflets [11, 12]. In these experiments, tethers were formed using gravitational force on glass beads or an additional pipette to retract a tether at a constant rate from an aspirated vesicle. In an alternative approach, magnetic forces have been used to pull tethers. Heinrich and Waugh used a large electromagnet based upon an iron core wrapped with a solenoid in order to pull tethers off aspirated vesicles and measure the membrane bending stiffness [13]. Hosu and Forgacs pulled tethers off adhered cells to study the effect of specific and nonspecific interactions in the tether formation process [14]. While tethers can be successfully pulled with a large iron-core electromagnet, such a device is bulky, produces a force profile that is difficult to model, and has a large inductance that can limit the force modulation bandwidth to the order of 10^2 Hz [15].

To address these limitations, we constructed a magnetic force transducer using microfabrication methods. Microfabricated devices have very low inductances that allow modulation of forces at frequencies several orders of magnitude faster than their larger counterparts [15]. In our design, the device is straightforward to construct with standard photolithographic techniques, compact, inexpensive and easily integrated into standard microscopes. The force profile is also simple to model. Although microfabricated magnetic force transducers have been described before [15–20], they have not been integrated with micropipette techniques and used to measure membrane mechanical properties.

Below, we describe the MMFT device and present a detailed characterization of its magnetic force and thermal properties. We demonstrate the ability to form tethers from GUVs, and we measure threshold forces and tether dynamics. The thermal properties of the device are used to accurately measure the thermal expansivity coefficient of the membrane. This MMFT-aspiration system is easy to operate and broadly applicable to a variety of molecular and cell mechanical experiments, and it is especially attractive as a straightforward method for the controlled application of dynamic forces.

5. Materials and Methods

5.1. Magnetic Force Transducer Fabrication

Following standard photolithographic techniques [21], we fabricated gold wires atop c-axis cut sapphire (1.5″ × 2″ × 1 mm, Swiss Jewel, Philadelphia, PA) [22]. Briefly, the sapphire was cleaned in a 10:1 (v/v) H_2SO_4:H_2O_2 Piranha etch followed by standard organics. Remaining moisture was removed via a 100°C bake for 30 min. Two seed layers were evaporated onto the substrate using a Sharon E-beam evaporator: 100 Å of 99.99% Ti at a rate of 1 Å s^{-1}, and 1000 Å of 99.999% Au (Cerac, Milwaukee, WI) at 2 Å s^{-1}. To form boundaries of the gold wire during electroplating, a 40-μm thick layer of SU-8 2015 photoresist (Microchem, Newton, MA) was spun onto the sapphire substrate, with assistance of Omnicoat (Microchem), and soft-baked. After baking, the resist was exposed to UV light using an MJB4 Mask Aligner (Süss MicroTec, Philadelphia, PA) through a patterned chrome mask (designed in house, made by Fineline Imaging, Colorado Springs, CO). A post-exposure bake followed. The guide channels were finally formed upon development of the photoresist.

A 25 μm thick layer of gold was plated onto the exposed portions of the seeding layer over 25 hr. The layer was formed with a current density of 0.275 mA cm^{-2} passing through the chip while submerged in a Techni-Gold 25 ES Au solution (Technic Inc., Cranston, RI) at 60°C while being stirred at 220 rpm. The SU-8 2015 and Omnicoat were then removed with Remover PG (Microchem). Exposure to a GE-8110 KI:I_2 gold etchant (Transene, Inc., Danvers, MA) for 50 sec etched the seed layer while not significantly reducing the gold on the electroplated wires. Using a profiler (Dektak 6M, Veeco, Plainview, NY), we determined the wires were 90 μm wide and 25 μm tall. Figure 1 shows a central portion of a sapphire chip with six gold wires—for redundancy—and leads for application of currents to generate a magnetic field. Up to 6 A could be applied to the device for up to 5 s without destroying the gold wires, but 3 A or less were generally applied in experiments to avoid excessive heating. The device cost a few hundred dollars to fabricate—with the main cost being that of the gold. In addition to a low cost compared to many other force application systems, MMFT devices of various patterns are possible, limited to the geometry and resolution of the chrome mask. Furthermore, a new device may be fabricated within two days. As such, it is quick and inexpensive to modify the system. Additionally, as the sapphire substrate can be patterned and biofunctionalized [23], the MMFT can be used to apply forces to vesicles or cells adhered to the functionalized substrate. To affix the sapphire piece, a copper stage holder was machined and fit snugly into an inverted Zeiss microscope. A polydimethylsiloxane (PDMS, Dow Corning) chamber was placed over the device to

minimize fluid evaporation. This chamber held in the sample solution through surface tension and had access on one side for a micropipette.

5.2. Vesicle Formation

The majority of vesicles were formed using the electroformation technique described by Zhou and Raphael [24, 25]. A 15 μL chloroform solution containing 1 mg mL^{-1} 1-stearoyl-2-oleoyl-*sn*-glycero-3-phosphatidylcholine (SOPC) or, in the case of tether experiments, 1-palmitoyl-2-oleoyl-*sn*-glycero-3-phosphocholine (POPC, both from Avanti Polar Lipids, Alabaster, AL), which had been stored at −20°C under nitrogen, was spread on each of two platinum electrodes and placed under vacuum for at least 2 hr. The electrodes were then submerged in 200 mM sucrose solution (Sigma-Aldrich, St. Louis, MO) and exposed to an alternating voltage. The voltage consisted of the waveforms: 10 Hz at 250 mV to 1000 mV in 250 mV increments, at 10 min each; then 6.6 Hz at 750 V and 3.3 Hz at 500 mV, at 10 min each; finally 1.1 Hz at 250 mV for 90 min. The vesicles were then collected and stored under nitrogen in a 4°C refrigerator. For tether experiments, either 0.5 mol % or 5 mol % Biotin-X-NHS (EMD Chemicals, San Diego, CA) was added to the SOPC solution.

5.3. Magnetic Bead Composition

Paramagnetic beads (Spherotech, Lake Forest, IL) at 2.5% w/v were stored in 0.016 M PBS, pH 7.4 with 0.02% sodium azide. These 2.2 μm diameter beads consisted of a 12% v/v γ-Fe_2O_3 nanoparticle-polystyrene blend. Streptavidin-coated ferromagnetic beads (Spherotech) at 1% w/v were also contained in 0.016 M PBS, pH 7.4 with 0.02% sodium azide, and the 4.4 μm diameter microspheres consisted of an 8% v/v CrO_2 nanoparticle-polystyrene blend. The beads were diluted ten times, thoroughly mixed, and refrigerated. For force calibration experiments, a 2 μL stock bead solution was further diluted in 998 μL Milli-Q deionized water. For tether experiments, the 2 μL bead solution was mixed in a solution composed of 998 μL 210 mM glucose (Sigma-Aldrich) and 12.5 μL 10x PBS. Immediately before experiments, the ferromagnetic beads were exposed to a 300 mT field for at least 5 seconds to align the magnetic microdomains within the beads. Only 200 mT is needed to ensure maximum remanent magnetization [26].

5.4. Vesicle Aspiration

Aspiration pipettes were fabricated using a P-97 micropipette puller (Sutter Instrument, Novato, CA) on borosilicate capillary tubes (Kimble Chase, Vineland, NJ) and cut cleanly on a custom-built microforge. A 1% bovine serum albumin (Sigma) solution in 210 mM glucose was used to coat the pipettes, which were subsequently washed in a pure glucose solution. During experiments, pressure was maintained by attaching the micropipette to a water reservoir with 0.01 mm resolution (Robo Cylinder, IAI, Torrance, CA) and the height of the water reservoir corresponding to a neutral pressure at the pipette tip was periodically calibrated using vesicle debris or magnetic beads, both of which experienced neutral pressures at the same water reservoir height. Pressures from 4.9 to 49 Pa were then used to aspirate the vesicle within the pipette.

5.5. Force Calibration of MMFT

Force calibration of the MMFT was conducted on an Axiovert 200M inverted microscope on a 20x Ph1 LD A-Plan (Zeiss, Thornwood, New York) with a 1.6x optovar. After beads were added, and if necessary, magnetized, a 1 s current pulse of 0.5 A to 3 A was sent through a single wire on the MMFT via a custom-built computer interface. These high currents generated a magnetic field that decreased with distance from the wire. Any magnetic microbeads in the system experienced a force of attraction and were accelerated towards the wire. Figure 2(a) depicts a cartoon of the device.

Images were taken with a Retiga 2000R (Qimaging, Surrey, BC) at 4×4 binning and with external triggering via Labview 2009 (National Instruments, Austin, TX) to obtain frame rates of up to ~50 fps. Images were subsequently analyzed with custom tracking programs in MatLab 2009b (The Mathworks, Natick, MA) to obtain particles trajectories and velocities.

The expected force profile is easily calculated from the known cross-sectional geometry of the wire, treating it as an infinitely long rectangular wire with uniform current density. We integrated the field, $\vec{B}$, generated by the current, I, as:

$$\vec{B}(\vec{r}) = \frac{\mu_0 I}{2\pi A} \int\int_A dA \frac{1}{|\vec{r} - \vec{r}_0|} \hat{\varphi}, \quad (1)$$

where μ_0 is the permeability of free space, A is the cross-sectional area of the wire normal to the current flow, $\vec{r}$ is the position of the bead, and $\vec{r}_0$ is the location of infinitesimal element of the cross-sectional area. The integral extends over the wire cross section lying in a plane perpendicular to the wire and containing the location of the bead. Figure 2(b) shows the result of this calculation along the $+y$ direction at the wire's mid-height. The field is fit well by the equivalent expression for an infinitely thin wire:

$$B = \frac{\mu_0 I}{2\pi y} \hat{y}, \quad (2)$$

where y is the distance from the center of the wire. We used this expression for the field in all force calibration measurements.

5.6. Thermal Characterization of the MMFT

5.6.1. Finite Element Modeling—The temperature profile within the device was modeled using the Transient Heat Transfer Conduction package on COMSOL 3.4. All components of the MMFT system were included in the model: the sapphire, gold wires, surrounding air, and PDMS and glass coverslip chamber filled with water. The model used time step sizes of no more than 0.01 sec and contained over 140,000 mesh points. The model's outer boundaries were modeled with large enough spatial dimensions as to not affect the model's convergence; increasing the dimensions of the model's outer boundaries had negligible effect on the temperature profile. These outer boundaries were set so that they were closer to the wire than the boundaries in the real system. Additionally, each outer

boundary's temperature was held at 293.15 K, and at all interior boundaries, the temperature was continuous. The heat source for the model was determined experimentally by measuring the voltage drop across the wire between the pads for each applied current and assuming that the dissipated power (IV) was deposited uniformly in the wire. The heat source in the model was only present during the first 6 s of the simulation, while the simulation itself lasted up to 16 s, which matched experimental conditions. Swiss Jewel provided the thermal conductivity (32.5 W m^{-1} K^{-1}), density (3970 kg m^{-3}), and heat capacity of sapphire (669.44 J kg^{-1} K^{-1}), and the parameters of PDMS were taken from the Polymer Data Handbook [27]. All other material parameters were from the COMSOL materials database.

5.6.2. Membrane Thermoelasticity—The area of the GUV membrane and the length of projection into the pipette are sensitive to the temperature of the local environment. Determination of projection lengths into the pipette of an aspirated vesicle was performed with a 40x DIC W Plan-Apochromat (Zeiss) with a 1.6x optovar at 1×1 binning and frame rates of ~28 fps. The projection length changed with current due to temperature rise of the membrane. The strain resulting from this temperature rise, α, was determined using

$$\alpha = \frac{2R_P \Delta L\,(1 - R_P/R_V)}{4R_V^2 - R_P^2 + 2R_P L_0}, \quad (3)$$

where R_p is the pipette radius, R_v is the vesicle radius, ΔL is the change in projection length, and L_0 is the initial projection length [25, 28]. Using the COMSOL model of the temperature rise of the MMFT during current pulses lasting 6 s of 1, 2, or 3 A, a thermal area expansitivity of the membrane was extracted from the observed strain.

5.7. Tether Studies

Tether studies consisted of first aspirating vesicles as described above (see figure 2(a)). The vesicle was then slowly moved to a free-floating bead and tapped against it until the streptavidin-coated bead adhered to the biotinylated Biotin-X lipids within the GUV. The GUV-bead complex was then gently moved to within 100 μm of the MMFT. A ramp waveform (1, 2, or 3 A for 3 or 6 s) was applied, and the resulting images were analyzed to obtain tether extension curves.

6. Results and Discussion

6.1. Force Calibration

In order to verify our field profile and calibrate the force on the beads, we tracked the response of both paramagnetic and ferromagnetic microspheres, not attached to vesicles, as current was passed through the magnetic force transducer. The beads were in the low Reynolds number regime, so the velocities of the tracked particles were converted into forces using Stokes Law:

$$\vec{F}_{Stokes} = -6\pi\eta r\vec{v}, \quad (4)$$

where F_{Stokes} is the Stokes force, η the viscosity of water (0.89 mPa s), r the radius of the bead, and v the velocity. The Stokes force balanced the applied magnetic force $\vec{F}_{Stokes} = -\vec{F}_{mag}$.

For a magnetic bead, the force due to an applied magnetic field is given as

$$\vec{F}_{mag} - \nabla(\vec{m} \cdot \vec{B}), \quad (5)$$

where m is the magnetic moment of the bead. For a paramagnetic bead with a magnetic susceptibility χ_{bead} and radius R [19], (5) reduces to

$$\vec{F}_{para} = -\frac{\mu_0 \chi_{bead} R^3}{3\pi} \frac{I^2}{y^3} \hat{y}. \quad (6)$$

As can be seen in figure 3 (a), the force on free floating paramagnetic beads follow a y^{-3} master curve over a current range from 0.75 A to 3 A when normalized by the current squared. The maximum force seen for paramagnetic beads in this study was 5.4 pN. Taking the parameters of the fit curve and a bead radius of 1.1 μm, we found a χ_{bead} of 0.14. This value compares well to the susceptibility of 0.17 reported by Shevkoplyas *et al.* for superparamagnetic microbeads composed of iron oxide in a polymer matrix when applying (6). The discrepancy between the values may be due to slightly different filling fractions between bead types, leading to different force strengths for similarly sized beads. Similarly, given the strong dependence on the radius, slight difference in bead size will yield different estimates in the susceptibility.

Applying (5) to a free-floating ferromagnetic bead, the force experienced is

$$\vec{F}_{ferro} = -\frac{\mu_0 m}{2\pi} \frac{1}{y^2} \hat{y}. \quad (7)$$

Figure 3(b) shows the force profiles of ferromagnetic beads normalized to I when exposed to fields generated by currents ranging from 0.5 A to 3 A. The maximum force seen for ferromagnetic beads was ~20 pN, which is comparable to the forces applied using an iron-core-based electromagnet [13]. The low forces recorded for 3 A might have been due to non-negligible convective effects at higher current. Calibration at 3A is also difficult due to high bead velocity. Other than at 3 A, these profiles fit a y^{-2} curve well, and yield a magnetic moment of 4×10^{-14} A m^2. While the magnetic moment depends upon volume fraction and

magnetization of the magnetic material, our measured value agrees reasonably well with a previously reported value of 3×10^{-13} A m^2 extrapolated from SQUID magnetometer results for similar beads [26]. Ferromagnetic beads were used for the biophysical studies in this work because larger applied forces were possible and the force profile did not decrease with distance as quickly as compared to paramagnetic beads. While paramagnetic beads had some practical advantages, including not requiring magnetization before use and of having magnetic moments that modulated linearly with external field in the field strengths of interest, the lower applied forces limited the use of paramagnetic beads for membrane tether studies. However, the calibration data on paramagnetic beads substantiates the quantitative calculation of forces in the device because different spatial dependence of the force provided an independent check of the expected magnetic field profile.

While forces of ~20 pN observed with ferromagnetic beads are not as high as those achievable with optical tweezers or macroscopic magnetic transducers, they are large enough to conduct mechanical studies on vesicles or cell membrane blebs. Higher forces further from the wire would enable the study of longer tether lengths (> 100 μm) and measurement of the nonlocal bending energy of the membrane [11, 12] and investigation of the electromechanical properties of membranes under high curvature [29]. In principle, the forces may be increased by using beads of higher magnetic content or by increasing the current that the device can carry. Although thermal concerns limit the electrical current in the MMFT described herein, the MMFT design can be modified to roughly double the current limit based on our understanding of the thermal response of the device, which is described below. While it may be possible to increase the forces with optimization of bead properties, we have focused on our ability to apply controllable and calibrated forces rather than on investigating the magnetic properties of the beads.

6.2. Membrane Thermoelasticity

As in several other force application techniques, such as optical tweezers [30–33] and some magnetic designs [18], the MMFT described here can cause localized heating of the solution bathing the membrane system. In this case, it is due to current flow producing Joule heat, which raised the temperature of the water near the wire and the vesicle. This temperature rise caused the membrane area to expand, which manifested itself as a visible increase in the projection length. In order to study this phenomenon carefully, we applied a 6 s constant current pulse through the MMFT at various current levels (1 A, 2 A, and 3 A). At the onset of current application, the projection length increased rapidly for the first few hundred milliseconds, and then grew more gradually, as can be seen in figure 4(a). When the current halted, the projection length returned to its initial extension with a similar temporal pattern.

In order to understand the response of the vesicle, the temperature of the system was modeled using COMSOL 3.4, as detailed in section 5.6.1. The result of this model may be seen as the dashed lines in figure 4(b). The temperature rise followed the I^2 dependence expected for Joule heating, with a maximum temperature rise of 30°C after 6 s with $I = 3$ A. At 2 A after 3 s, the maximum current at which the majority of experiments were conducted and the length of time for which most experiments took place, the temperature rise was ~10°C, which resulted in nearly physiological temperatures and was only a factor of two

greater than the heating reported in optical tweezers [30, 32]. Using larger wires, the Joule heating could be further reduced. The temperature rise was described by a double exponential with a fast time constant of 0.3 s and slow time constant of 3 s. Likewise, cooling followed a double exponential with time constants of 0.4 s and 4 s. The fast time constant related to the immediate warming of the solution and sapphire; the slow time constant corresponded to the gradual increase in the background temperature as the entire sapphire chip heated. The inset shows the position dependence of temperature and one can see that the temperature was relatively uniform in the region of interest (ROI) for our experiments (between 25 μm and 100 μm), with a variation of less than 2°C for 2 A. This uniformity is chiefly due to the high thermal conductivity of the sapphire substrate.

The ratio of area change to temperature change is the thermal area expansivity modulus (α_T) of the membrane. Using α_T as a free parameter, we were able to match all the measurements of the areal strain in the vesicle to COMSOL temperature predictions (error bar plots in figure 4(b)). This fit yields a thermal area expansivity modulus of SOPC GUVs of 1.7 ± $0.4x10^{-3}K^{-1}$. To our knowledge, this is the first determination of the area expansivity of SOPC, but the obtained value is reasonable as it falls between the values of $2.4x10^{-3}K^{-1}$ measured in egg lecithin [28] and $1.2x10^{-3}K^{-1}$ reported for red blood cells [34]. Given that the elastic modulus of egg lecithin (0.14 N m^{-1}, [28]) is less than that of SOPC (0.211 N m^{-1}, [24]), which in turn is less than that of red blood cells (0.45 N m^{-1}, [34]), the thermal area expansivity of SOPC is expected to lie between that of egg lecithin and red blood cells. Thus, using knowledge of the temperature change from the COMSOL model, the MMFT can be used to determine α_T for aspirated membrane systems, or conversely, an aspirated vesicle can be used to determine the local temperature increase at microscale length scales if the expansivity modulus of the vesicle is known.

The uncertainty in our measurement of α_T was dominated by systematic uncertainty in the results of the COMSOL model. The major contributions to uncertainty in the predicted temperature change were uncertainty in sapphire conductivity, and variation in the applied power, which changed slightly because the resistivity of the wire increased as the temperature rose. By running simulations at the extremes of these parameters, we estimated a relative error of 20% as the uncertainty in the computational model.

6.3. Membrane Tether Formation

In order to demonstrate the ability of the MMFT to study membrane mechanics, we conducted tether formation experiments by attaching ferromagnetic beads to micro-aspirated GUVs and tracking their position while applying a linear current ramp to the MMFT. Once the magnetic force reached sufficient strength, a tether formed, as seen in figure 5(a) for a representative tether, and continued to lengthen until the current stopped. At that time, the tether retracted, drawing the bead back to its original position. The length of the tether, L_t (figure 5(b)) was time dependent.

This trajectory may be seen in figure 5(c). The force on the bead increased linearly with current while the bead was stationary, but when the force reached 2.4 pN, a tether formed. The bead then moved toward the wire, which also caused an increase in the force rate experienced by the bead. At 3.2 s, the current stopped. Such trajectories are a powerful tool

for studying membrane properties, including determining the force at which tether formation occurs. We found that the force threshold, F_{th}, depended upon the concentration of biotin-X in the vesicle. At 0.5 mol % biotin-X, 2.1 ± 0.3 pN was required to pull a tether; while at 5 mol % biotin-X, 18.8 ± 5.4 pN was necessary. The adhesion strength depends upon membrane tension, the contact area and the concentration of receptors and ligands [5]. As the membrane tension was held approximately constant in our experiments, the greater required threshold force for higher biotin concentration likely reflects a greater contact area mediated by more adhesion sites between the streptavidin-coated ferromagnetic microbead and the biotinylated lipids, similar to previous observations in which the contact area was directly modulated [35].

Furthermore, with the ability to control piconewton forces dynamically, the effect of the force rate df/dt on tether formation can be investigated, which has not been carefully probed experimentally to the best of our knowledge. Control of df/dt is essential for understanding interactions mediated by specific receptor-ligand interactions, where the disassociation rate depends heavily on the rate of force application and molecular details of the bond [6, 36, 37]. In this work, we observed tether formation at rates of 7.6 ± 1.9 pN s^{-1} for 5% biotinylated lipids and of 1.59 ± 0.25 pN s^{-1} for 0.5% biotinylated lipids. However, our MMFT is capable of controlling force rates up to the order of 1×10^4 pN s^{-1} (data not shown) and so could be used for dynamic force spectroscopy of receptor-ligand interactions [37] by tailoring membrane and bead composition appropriately [6].

Returning to figure 5(c), the viscous force during tether return was driven by membrane tension and retarded by viscous drag. During the return, the bead experienced no external force as the magnetic field was turned off. The return itself was fairly constant as evidenced by the linear trajectory during this phase. In equilibrium tether systems, this force, F_{return}, is simply related to the bending stiffness and membrane tension by $F_{return}=2\pi\sqrt{2k_c\tau}$, where τ is the tension and k_c is the bending modulus [11, 38]. However, in dynamic systems, Evans and Yeung found that viscous dissipation between the membrane leaflets is significant [12]. Following previous developments [11, 12], the interlayer drag coefficient, b, can be calculated using the return force by

$$F_{return}=2\pi\sqrt{2k_c\tau}+2\pi\frac{dL_t}{dt}h^2\ln(R_V/R_t)\,b, \quad (8)$$

where h is the membrane thickness, R_V is the vesicle radius, and R_t is the tether radius. The second term on the right, the viscous term, may contribute up to the same order of magnitude as the first term, the tension term, to the total force [11, 12], and so cannot be neglected. Using $k_c = 1.2x10^{-19}$ J [11] and $R_t = 20$ nm we obtained a value of $b = 1.1x10^9\pm0.5x10^9$ N s m^{-3}. (Note that although R_t was not measured independently, the calculated value of b only depends weakly on R_t). This is comparable to a value of $b = 4.6x10^8$ N s m^{-3} measured by Raphael and Waugh [11] and the 10^8 magnitude estimate of Evans and Yeung for PC systems [38]. The interlayer membrane viscosity may be sensitive to the rate at which the tether flows, which can also be probed using the MMFT.

7. Conclusion

We have developed a microfabricated magnetic force transducer (MMFT) that can be combined with microaspiration in order to study membrane mechanical properties via the application of point forces to the membrane. In this design, the transducer's magnetic field is straightforwardly modeled, and its field strength is adjusted by controlling the current passing through the wire. The ability to precisely control the current enables application of force rates from 1 to 10^4 pN s^{-1} and application of various waveforms, including force ramps, pulses and sinusoids. The range of force profiles achievable in the MMFT is difficult to reproduce in other force application systems.

To demonstrate the utility of the MMFT, several biophysical properties of giant unilamellar vesicles were measured: the thermal expansivity coefficient α_T, the threshold force for tether formation F_{th}, and the interlayer drag coefficient b. For SOPC vesicles, we found $\alpha_T = 1.7 \pm 0.4x10^{-3}$ K^{-1} in the temperature range of 22 to 50°C, $F_{th} = 2.1 \pm 0.3$ to 18.8 ± 5.4 pN, depending on the concentration of biotin in the vesicle, and $b = 1.1 \pm 0.6x10^9$ N s m^{-3}. All these properties are consistent with previous measurements, establishing the MMFT-microaspirator as a powerful tool for studying membrane mechanical properties. For example, the MMFT can be used to quantitatively determine how changes in the chemical composition of the membrane by biologically important molecules—such as cholesterol, salicylate, or alcohols—alter the dynamic properties of membranes. In addition, different receptor-ligand pairs can be studied, and the MMFT can be used to determine the relationship between density of adhesion sites and force thresholds and to investigate the relationship between dynamic force application and adhesion strength.

Acknowledgments

We thank Shinji Strain for his help in validating the thermal cause of the vesicle expansivity. We also acknowledge funding from NSF GRFP, NSF CAREER (CBET-0449379), the Hamill Innovation Grant, and partial support from both a NIH Molecular Biophysics Training Grant (T32 GM008280) and a NIH Nanobiology Training Grant (T90 DK70121-04).

Bibliography

1. Ingber DE. Cellular mechanotransduction: Putting all the pieces together again. FASEB. 2006; 20:811–27.
2. Neuman KC, Nagy A. Single-molecule force spectroscopy: Optical tweezers, magnetic tweezers and atomic force microscopy. Nat Methods. 2008; 5:491–505. [PubMed: 18511917]
3. Rocha MS, Mesquita ON. New tools to study biophysical properties of single molecules and single cells. An Acad Bras Cienc. 2007; 79:17–28. [PubMed: 17401470]
4. Neuman KC, Block SM. Optical trapping. Rev Sci Instrum. 2004; 75:2787–809. [PubMed: 16878180]
5. Smith A-S, Seifert U. Vesicles as a model for controlled (de-)adhesion of cells: A thermodynamic approach. Soft Matter. 2007; 3:275–89.
6. Merkel R, Nassoy P, Leung A, Ritchie K, Evans E. Energy landscapes of receptor-ligand bonds explored with dynamic force spectroscopy. Nature. 1999; 397:50–3. [PubMed: 9892352]
7. Hochmuth RM, Mohandas N, Blackshear PL. Measurement of the elastic modulus for red cell membrane using a fluid mechanical technique. Biophys J. 1973; 13:747–62. [PubMed: 4726877]
8. Hochmuth RM, Waugh RE. Erythrocyte membrane elasticity and viscosity. Annu Rev Physiol. 1987; 49:209–19. [PubMed: 3551799]

9. Hochmuth RM, Wiles HC, Evans EA, McCown JT. Extensional flow of erythrocyte membrane from cell body to elastic tether. Ii. Experiment. Biophys J. 1982; 39:83–9. [PubMed: 7104454]
10. Waugh RE, Song J, Svetina S, Zeks B. Local and nonlocal curvature elasticity in bilayer membranes by tether formation from lecithin vesicles. Biophys J. 1992; 61:974–82. [PubMed: 1581506]
11. Raphael RM, Waugh RE. Accelerated interleaflet transport of phosphatidylcholine molecules in membranes under deformation. Biophys J. 1996; 71:1374–88. [PubMed: 8874013]
12. Evans EA, Yeung A. Hidden dynamics in rapid changes of bilayer shape. Chem Phys Lipids. 1994; 73:39–56.
13. Heinrich V, Waugh RE. A piconewton force transducer and its application to measurement of the bending stiffness of phospholipid membranes. Ann Biomed Eng. 1996; 24:595–605. [PubMed: 8886240]
14. Hosu BG, Sun M, Marga F, Grandbois M, Forgacs G. Eukaryotic membrane tethers revisited using magnetic tweezers. Phys Biol. 2007; 4:67–78. [PubMed: 17664652]
15. Fisher J, Cribb J, Desai K, Vicci L, Wilde B, Keller K, Taylor R, Haase J, Bloom K, O'Brien E, et al. Thin-foil magnetic force system for high-numerical-aperture microscopy. Rev Sci Instrum. 2006; 77:023702.
16. de Vries CR, Kanger J, Krenn B, van Driel R. Patterned electroplating of micrometer scale magnetic structures on glass substrates. J Microelectromech S. 2004; 13:391–5.
17. Henighan T, Chen A, Vieira G, Hauser AJ, Yang FY, Chalmers JJ, Sooryakumar R. Manipulation of magnetically labeled and unlabeled cells with mobile magnetic traps. Biophys J. 2010; 98:412–7. [PubMed: 20141754]
18. Lee H, Purdon AM, Westervelt RM. Manipulation of biological cells using a microelectromagnet matrix. Appl Phys Lett. 2004; 85:1063–5.
19. Shevkoplyas SS, Siegel AC, Westervelt RM, Prentiss MG, Whitesides GM. The force acting on a superparamagnetic bead due to an applied magnetic field. Lab Chip. 2007; 7:1294–302. [PubMed: 17896013]
20. Drndic M, Johnson KS, Thywissen JH, Prentiss M, Westervelt RM. Micro-electromagnets for atom manipulation. Appl Phys Lett. 1998; 72:2906–8.
21. Drndic, M. Micro-electromagnets for particle control. 2000.
22. Stark, DJ. Master's Thesis. William Marsh Rice University; Houston, TX: 2009. The use of a microelectroporator to study poration of jurkat cells.
23. Stutzmann M, Garrido JA, Eickhoff M, Brandt MS. Direct biofunctionalization of semiconductors: A survey. Physica Status Solidi (A) Applications and Materials. 2006; 203:3424–37.
24. Zhou Y, Raphael RM. Effect of salicylate on the elasticity, bending stiffness, and strength of sopc membranes. Biophys J. 2005; 89:1789–801. [PubMed: 15951377]
25. Zhou Y, Raphael RM. Solution ph alters mechanical and electrical properties of phosphatidylcholine membranes: Relation between interfacial electrostatics, intramembrane potential, and bending elasticity. Biophys J. 2007; 92:2451–62. [PubMed: 17172308]
26. Behrend C, Anker J, McNaughton B, Kopelman R. Microrheology with modulated optical nanoprobes (moons). J Magn Magn Mater. 2005; 293:663–70.
27. Mark EJ. Polymer data handbook. 2009:1250.
28. Kwok R, Evans E. Thermoelasticity of large lecithin bilayer vesicles. Biophys J. 1981; 35:637–52. [PubMed: 7272454]
29. Glassinger E, Lee AC, Raphael RM. Electromechanical effects on tether formation from lipid membranes: A theoretical analysis. Phys Rev E. 2005; 72:041926.
30. Peterman EJG, Gittes F, Schmidt CF. Laser-induced heating in optical traps. Biophys J. 2003; 84:1308–16. [PubMed: 12547811]
31. Li Z, Anvari B, Takashima M, Brecht P, Torres JH, Brownell WE. Membrane tether formation from outer hair cells with optical tweezers. Biophys J. 2002; 82:1386–95. [PubMed: 11867454]
32. Celliers PM, Conia J. Measurement of localized heating in the focus of an optical trap. Appl Opt. 2000; 39:3396–407. [PubMed: 18349909]

33. Mao H, Arias-Gonzalez JR, Smith SB, Tinoco I, Bustamante C. Temperature control methods in a laser tweezers system. Biophys J. 2005; 89:1308–16. [PubMed: 15923237]
34. Waugh R, Evans EA. Thermoelasticity of red blood cell membrane. Biophys J. 1979; 26:115–31. [PubMed: 262408]
35. Koster G, Cacciuto A, Derényi I, Frenkel D, Dogterom M. Force barriers for membrane tube formation. Phys Rev Lett. 2005; 94:068101. [PubMed: 15783778]
36. Nowak SA, Chou T. Models of dynamic extraction of lipid tethers from cell membranes. Phys Biol. 2010; 7:026002. [PubMed: 20453295]
37. Evans EA, Calderwood DA. Forces and bond dynamics in cell adhesion. Science. 2007; 316:1148–53. [PubMed: 17525329]
38. Evans E, Yeung A. Apparent viscosity and cortical tension of blood granulocytes determined by micropipet aspiration. Biophys J. 1989; 56:151–60. [PubMed: 2752085]

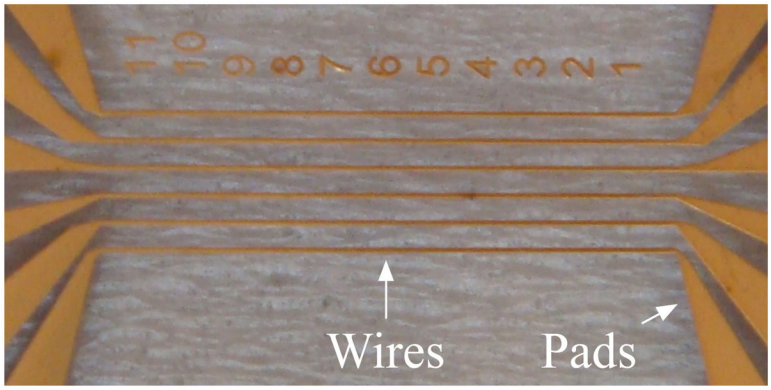

Figure 1.

Photograph of the MFT after microfabrication. The six gold wires are 9 mm long with a 425-μm center-center spacing. The pads enable the connection of the microscale wires to macroscale sources.

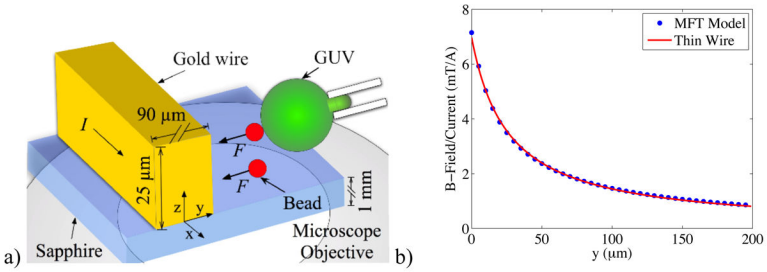

Figure 2.

Schematics of the MFT with an aspirated GUV and associated model of the magnetic field. a) An electroplated rectangular gold wire sits atop an optical quality sapphire substrate above the microscope objective. Current (*I*) in the wire generates a magnetic field that exerts force upon the ferromagnetic bead adhered to the GUV, which can pull a tether. Free-floating beads were used to calibrate forces. b) Calculated magnetic field versus distance from the wire edge at half the height of the wire. Even though the wire is rectangular, the field (blue dots) matches well the r^{-1} curve (red line) expected for an infinitely thin wire.

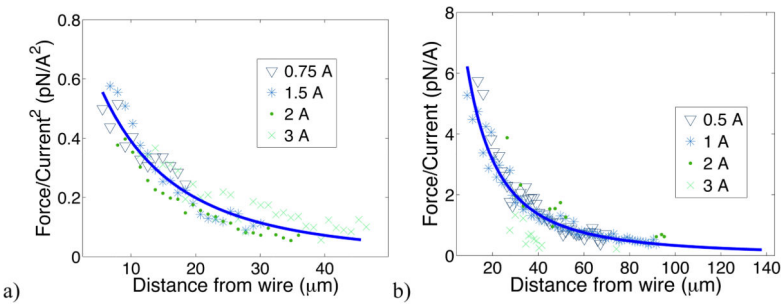

Figure 3.

Normalized magnetic forces generated by the MMFT measured using magnetic beads. a) The normalized force experienced by free floating paramagnetic beads for several different currents scales as the square of the current and varies with distance from the wire (r) as $\nabla(B^2) \propto r^{-2}$ (solid blue line), as expected for paramagnetic material. Each current is the binned average of several runs with a bin of 1 μm. b) The force for free floating ferromagnetic beads scale with the current and varies as $\nabla(B) \propto r^{-2}$ (solid blue line). Each current is the binned average of several runs with a bin of 1 μm.

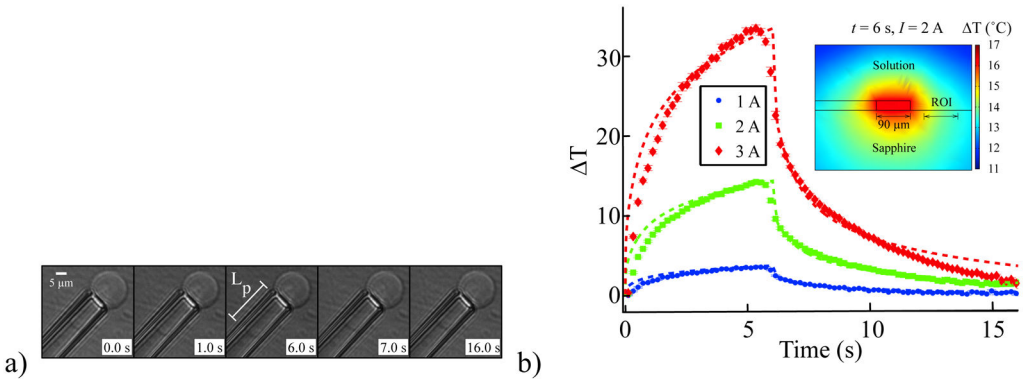

Figure 4.

Thermomechanical responses of aspirated vesicles in reaction to a 6 s pulse at 1, 2, or 3 A. a) A time sequence showing the increase in L_p as current is applied. Once the current stops flowing, the projection length quickly returns to its original value. b) The temperature estimate of the magnetic force transducer using a COMSOL model (dashed lines) shows an I^2 dependence with maximum temperature changes of 33°C at 3 A. Estimating the thermal area expansivity at $1.7x10^{-3}$ K^{-1}, the areal strain change of the vesicle with applied current may be converted into temperature changes (error bar plots of mean temperature with standard error with symbols serving as error bars if error bars are not displayed) for 1 A (N = 35), 2 A (N = 35), and 3 A (N = 30). The variation of temperature with position predicted by the COMSOL model may be seen in the inset with the solution of the model at t = 6 s with I = 2 A. The region of interest (ROI) depicts the range of positions of the GUVs during this study.

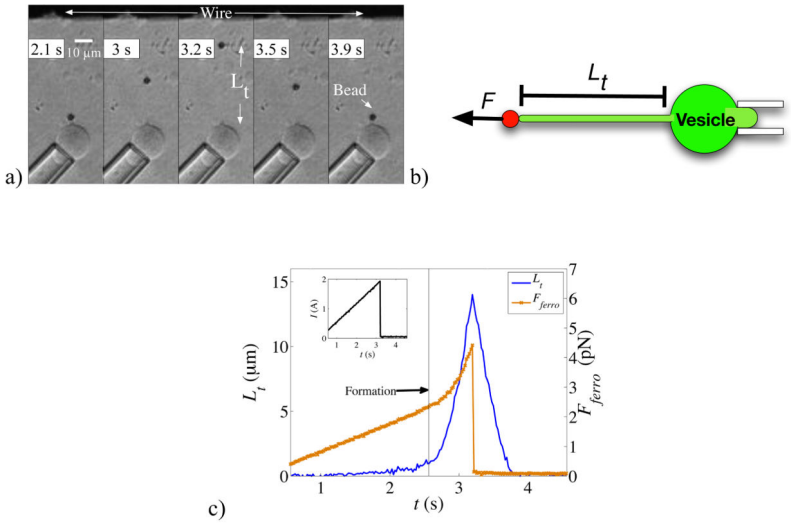

Figure 5.

Demonstration of a tether pulled from an aspirated GUV with the MMFT. a) The time sequence displays a ferromagnetic bead being pulled from a vesicle upon application of current through the wire. The current ramp increased linearly to 1, 2, or 3 A over 3 s. Once current flow was halted, the tether dragged the bead back to its initial position against the vesicle. b) A cartoon of the aspirated vesicle depicting the tether length, L_t, from the edge of the ferromagnetic bead to the vesicle surface. c) The trajectory (blue line) of L_t and pulling force, F_{ferro}, during the linear ramp (see inset) of the current to $I = 2$ A and sudden turn off of the current at $t = 3.2$ s. A tether ($L_t \sim 0$) was not formed until the force experienced by the ferromagnetic bead (brown line) was sufficiently high ($t \sim 2.6$ s). Once a tether formed, the force no longer followed a linear ramp since the distance to the wire was simultaneously decreasing. The force and force rate increased until the current, and hence force, was turned off. The rate of extension of the tether also amplified, as indicated by augmented slope, corresponding to the greater force experienced. The tether then retracted to its initial position solely under the influences of membrane forces and viscous drag from the medium as there was no magnetic force on the bead once the current flow ceased.